Structure of the ion acceleration region in cylindrical Hall thruster plasmas

Guentae Doh, Holak Kim, Dongho Lee, Sanghoo Park, Stéphane Mazouffre, Wonho Choe

Structure of the ion acceleration region in cylindrical Hall thruster plasmas

IOP Publishing J. Phys. D: Appl. Phys.
Journal **XX** (XXXX) XXXXXX https://doi.org/XXXX/XXXX

Structure of the ion acceleration region in cylindrical Hall thruster plasmas

Guentae Doh[1], Holak Kim[2], Dongho Lee[1], Sanghoo Park[3], Stéphane Mazouffre[4], and Wonho Choe[1,3*]
[1]Department of Physics, Korea Advanced Institute of Science and Technology (KAIST), 291 Daehak-ro, Yuseong-gu, Daejeon 34141, Republic of Korea
[2]Satellite Research Directorate, Korea Aerospace Research Institute, 169-84 Gwahak-ro, Yuseong-gu, Daejeon 34133, Republic of Korea
[3]Department of Nuclear and Quantum Engineering, KAIST, 291 Daehak-ro, Yuseong-gu, Daejeon 34141, Republic of Korea
[4]ICARE, CNRS, 1C avenue de la Recherche Scientifique, F-45100 Orléans, France

E-mail: wchoe@kaist.ac.kr

Abstract

We investigated the structure of the ion acceleration region and the shape of the ion velocity distribution function in cylindrical Hall thruster plasmas, using laser-induced fluorescence spectroscopy on Xe II metastable ions. On the thruster axis, the acceleration front is located deeper than a half-length of the discharge channel length, and the acceleration region reaches up to 3 times the discharge channel length (several centimeters) away from the channel exit, regardless of the discharge condition. It is noteworthy that ion acceleration mostly (more than 70%) takes place outside the discharge channel. The ion velocity distribution function is close to a single Gaussian inside the discharge channel. It however becomes substantially asymmetric when moving downstream. Double Gaussian distributions including cold and hot ion groups was in good agreement with the measured ion velocity distributions downstream with an R-squared greater than 0.995.

Keywords: Cylindrical Hall thruster, laser-induced fluorescence, acceleration region, ion velocity distribution function

1. Introduction

The structure of the ion acceleration region is of great importance in Hall thruster plasma research because it has a strong influence not only on ionization and acceleration but also on the performance and lifetime of thrusters. It is known that adjusting the anode voltage or propellant flow rate leads to a shift or modification of the electric field profile, and this behavior depends on the thruster geometry and the magnetic field topology [1-4]. The magnetic field is especially a key variable that can significantly affect the ion acceleration region. This is because the electric field is generally intense in the area where the strong radial magnetic field exists, and a downstream shift of the ion acceleration region by a magnetic shielding configuration has been identified [4-6].

Over the years, many changes in the geometry and magnetic field of the conventional annular Hall thrusters have been attempted for reducing the interaction between the plasma and walls, such as magnetically-shielded thrusters and wall-less thrusters [6, 7]. Particularly for miniaturization of Hall thrusters for low power operation, cylindrical Hall thrusters are considered advantageous because the removal of channel wall and magnetic components surrounding the thruster axis provides a reduced plasma surface-to-volume ratio [8]. In the cylindrical Hall thruster, the magnetic field is axially dominant near the thruster axis and the plasma is formed in a hollow cylindrical discharge channel. Therefore, the axial component as well as the radial component of the magnetic field plays an important role in electron confinement and transport [9]. Different behaviors compared to those of conventional annular Hall thrusters could be expected, and many unique physical features that are rarely seen in conventional annular Hall thruster plasmas have been reported. This includes a weak breathing-mode oscillation [8] and a high propellant utilization by a significant fraction of multiply-charged ions [10, 11]. Additionally, extended ion acceleration region up to more than 40 mm outside the discharge cavity as well as different electric potential profiles due to different magnetic field configurations was also reported [12]. However, the effect of the anode voltage and flow rate on the ion acceleration region and spatially-resolved internal measurement in cylindrical Hall thruster plasmas has not yet been fully addressed.

This study aims at investigating the structure of the ion acceleration region in cylindrical Hall thruster plasmas. The anode voltage and flow rate have been chosen as experimental variables. Ion velocity distribution functions (IVDFs) and ion energy profiles have been measured by laser-induced fluorescence (LIF) spectroscopy. The mean energy profile is used to estimate the structure of the ion acceleration region and to evaluate how the acceleration region depends on operating conditions. Furthermore, nonlinear ion acceleration is discussed by investigating the shape of IVDFs.

2. Experimental Setup

The schematic diagram of the Hall thruster used for the study is illustrated in Fig. 1(a), which is a typical cylindrical Hall thruster. Details can be found in previous papers [11, 13]. The discharge channel is 50 mm in diameter and 24 mm in depth. The magnetic field is produced by a pair of electromagnets whose current directions were the same, namely the co-current configuration. The operational conditions were varied either by changing the anode voltage in the range 200–350 V at a constant anode flow rate of 7.0 sccm, or by changing the anode flow rate in the range 4.0–10.0 sccm at a constant anode voltage of 300 V. The hollow cathode was operated with a 1.0 A keeper current at 1.0 sccm Xe flow rate. The cathode orifice was located at (r, z) = (60 mm, 10 mm) where r and z are the radial and axial coordinates, respectively, and (r, z) = (0, 0) corresponds to the thruster axis and exit plane. The magnetic field line intersecting the keeper orifice was represented as the dashed curve in Fig. 1(a). Experiments have been performed in a 3 m long and 1.5 m in diameter vacuum chamber. Four cryogenic pumps provide a

pumping rate of 24,000 L/s for Xe gas. Xenon gas was used as a propellant here and the operating pressure was maintained between 4–9 μTorr (corrected for Xe) at a flow rate of 5.0 – 11.7 sccm.

LIF spectroscopy is utilized to non-intrusively measure the IVDF of an atomic state [14, 15]. In this work, the Xe II ion is excited from the $5d^2F_{7/2}$ state to the $6p^2D^0_{5/2}$ state at 834.72 nm (in air). The resulting fluorescence due to the transition to the $6s^2P_{3/2}$ state can be observed at 541.9 nm (in air). A 110 mW output power continuous-wave tunable diode laser (Newport TLB 7115-01) with a 300 kHz bandwidth was employed as the excitation source. The laser beam first passes through a Faraday optical isolator (Newport ISO-08-800-BB) and a 9:1 beam splitter, as illustrated in Fig. 1(b). The small part of the split beam is focused onto a single-mode optical fiber that is coupled to a high-precision wavelength-meter for wavelength monitoring. The wavelength-meter (Newport WM1210) can resolve 1 pm with the accuracy of ±1 ppm in the near-infrared domain. The large part of the split beam is divided again by a 50:50 cube beam splitter to simultaneously measure the axial and radial velocity components of Xe II ions. The light intensity of the two laser beams is modulated at 500 Hz and 350 Hz using two mechanical choppers as can be seen in Fig. 1(b). The two beams are subsequently focused at the same location with a $f = 2.5$ m and a $f = 4$ m lenses, respectively, where f is the focal length. Inside the vacuum chamber, the fluorescence radiation produced by the two NIR laser beam is captured by means of a $f = 300$ mm lens. The lens makes a 58 degrees angle with respect to the thruster axis in such a way light can be collected inside the thruster channel. A set of mirrors guides the fluorescence outside the vacuum chamber to a $f = 500$ mm lens, which focuses the light onto the entrance slit of a monochromator (Chromex-500sm). The monochromator filters out the background radiations with a spectral width of 1.96 nm at 541.9 nm. A photomultiplier tube (Hamamatsu R7518P) is mounted at the exit slit of the monochromator to convert light into an electrical signal. As shown in Fig. 1(b), the light detector signal is sent to two lock-in amplifiers (Stanford Research Systems SR830) to simultaneously and independently measure the signals from the axial (500 Hz) and the radial (350 Hz) laser beams. The lock-in amplifier time constant was set at a 0.1 s with 24 dB/oct roll-off. Finally, a personal computer reads the output signal given by the two lock-in amplifiers.

Axial and radial LIF measurements have been performed, as indicated by the cross symbols "×" in Fig. 1(a). The size of the measurement volume is 0.6 mm × 1.2 mm × 1.3 mm for the axial laser beam and 0.6 mm × 1.2 mm × 2.8 mm for the radial beam, respectively. As a consequence, the optical power density of the axial and radial beams was 11.7 and 2.8 mW/mm^2, respectively. Previous studies reported the saturation of the optical transition as the source of uncertainty of LIF measurement [15-17]. To examine the suitability of the used beam power, we compared normalized IVDFs measured at $z = 60$ mm by varying the laser beam power density in the 1.2 to 14.5 mW/mm^2 range. The shape of IVDF was unchanged, which means that power broadening of the line shape is weak at such power densities and conclusions are not impacted. In other words, the Doppler broadening remains by far the main broadening mechanism.

The thruster and its hollow cathode were mounted on a motorized transition stage that could move 100 mm and 70 mm along the axial and radial direction, respectively. The measurement range was $z = -16 – 80$ mm and $r = 0 – 38$ mm. The excitation wavelength for Xe II ion at rest (null velocity) was evaluated. The fluorescence signals of the injected laser beam and of the counterpropagating beam reflected by the center surface of the thruster were recorded. The obtained excitation wavelength is 834.7234 ± 0.00014 nm (in air), where the measurement error indicates a 99% confidence interval that corresponds to ±50 m/s velocity.

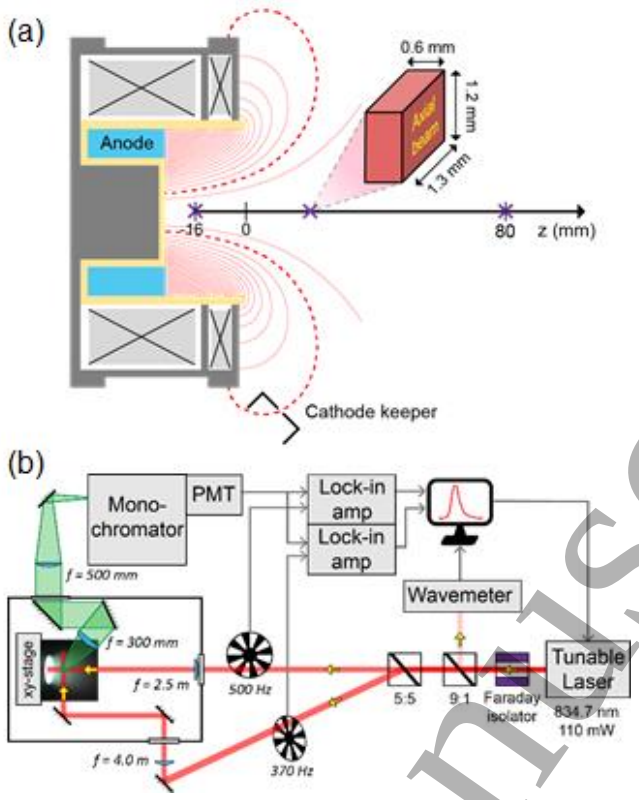

Figure 1. (a) A schematic diagram of the cylindrical Hall thruster used in these experiments and magnetic field lines. The '×' symbols denote the measurement points. The typical size of the sampling volume for LIF diagnostics was 0.6 mm × 1.2 mm × 1.3 mm. (b) Block diagram of the LIF spectroscopy setup. The detection range was z = -16 – 80 mm.

3. Experimental results

Figure 2 presents the measured axial and radial IVDFs at different axial positions at 300 V anode voltage and 7.0 sccm Xe flow rate. As shown in Fig. 2(a), the mean axial velocity increases from 6.6 to 18.5 km/s (peak velocity increases from 6.7 to 18.1 km/s) as Xe II ions move from z = -6 mm to 70 mm. On the other hand, the mean radial velocity, depicted in Fig. 2(b), stays around zero along the thruster axis. This result indicates that on the centerline ions are on average only accelerated in the z-direction over a long distance. The observation of significant ion acceleration from z = -6 mm to z = 70 mm in a cylindrical thruster plasma is remarkable because ion acceleration in conventional annular Hall thruster plasmas usually occurs only within 10 – 20 mm from the thruster exit plane [1, 18-20].

Figure 3(a) presents the measured mean ion velocity vector and mean ion energy of the cylindrical Hall thruster plasma at 300 V anode voltage and 7.0 sccm Xe flow rate in the axial-radial space. The mean axial and radial ion energies were obtained as $\overline{W}_z(z) = m\overline{v_z^2}/2 = \int mv_z^2/2 \times f_z(v_z)dv_z$ and $\overline{W}_r(z) = m\overline{v_r^2}/2$, respectively, where m is the ion mass, v_z and v_r are the axial and radial ion velocities, and $f_z(v_z)$ is the axial ion velocity distribution function. The ion trajectories and energy contours exhibit an upstream movement of the acceleration front and a narrowing of the acceleration region as moving away from the thruster axis. These results are considered to be related to the upstream shift of ionization location with the increase in radial component of the magnetic field [21]. It is also noteworthy that the electric potential contour significantly deviates from the magnetic field line in the

region where the magnetic field is axially dominant. Although the quasi-equipotential property along the magnetic field line does not hold for cylindrical Hall thrusters, such discrepancy was commonly found in other thrusters that have similar magnetic field configurations [12, 22]. With the assumption of isorotating electrons on the magnetic flux surface, it was shown that Hall current not only raises the inclination angle of magnetic field but also deflects the electric field so that it does not perpendicular to the magnetic field, and the deflection angle of the electric field could be nonnegligible for Hall thruster plasmas [23]. Therefore, ExB drifting electrons are thought to contribute to inconsistency between the potential contour and the magnetic field line. Figure 3(b), showing the electric potential measured by a floating emissive probe [21], demonstrates that the potential drop is still considerable even beyond z = 60 mm, as in Figure 3(a). In the figure, the white dashed lines represent the observation range to maintain low plasma perturbation (less than 2% discharge current variation).

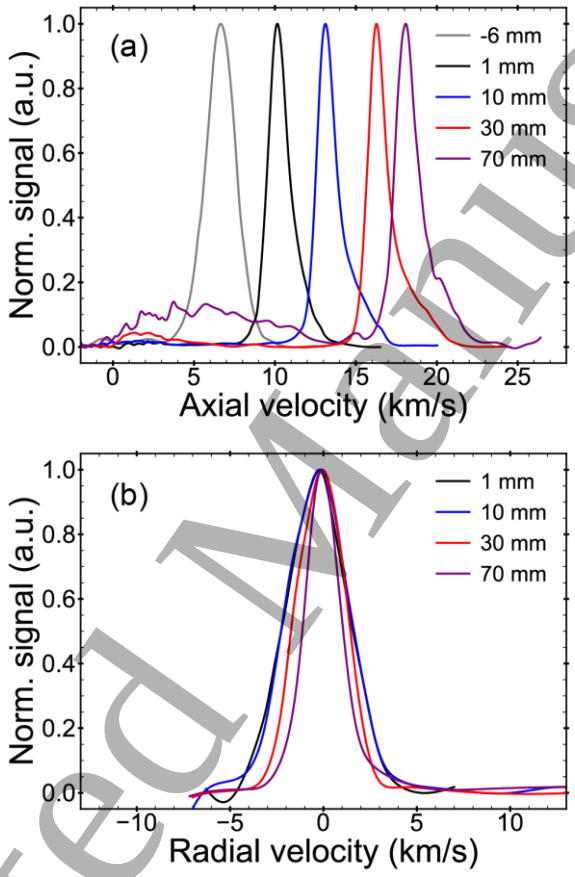

Figure 2. (a) The axial and (b) the radial IVDFs measured at z = -6, 1, 10, 30, and 70 mm, respectively. The operating conditions were 300 V anode voltage and 7.0 sccm anode flow rate.

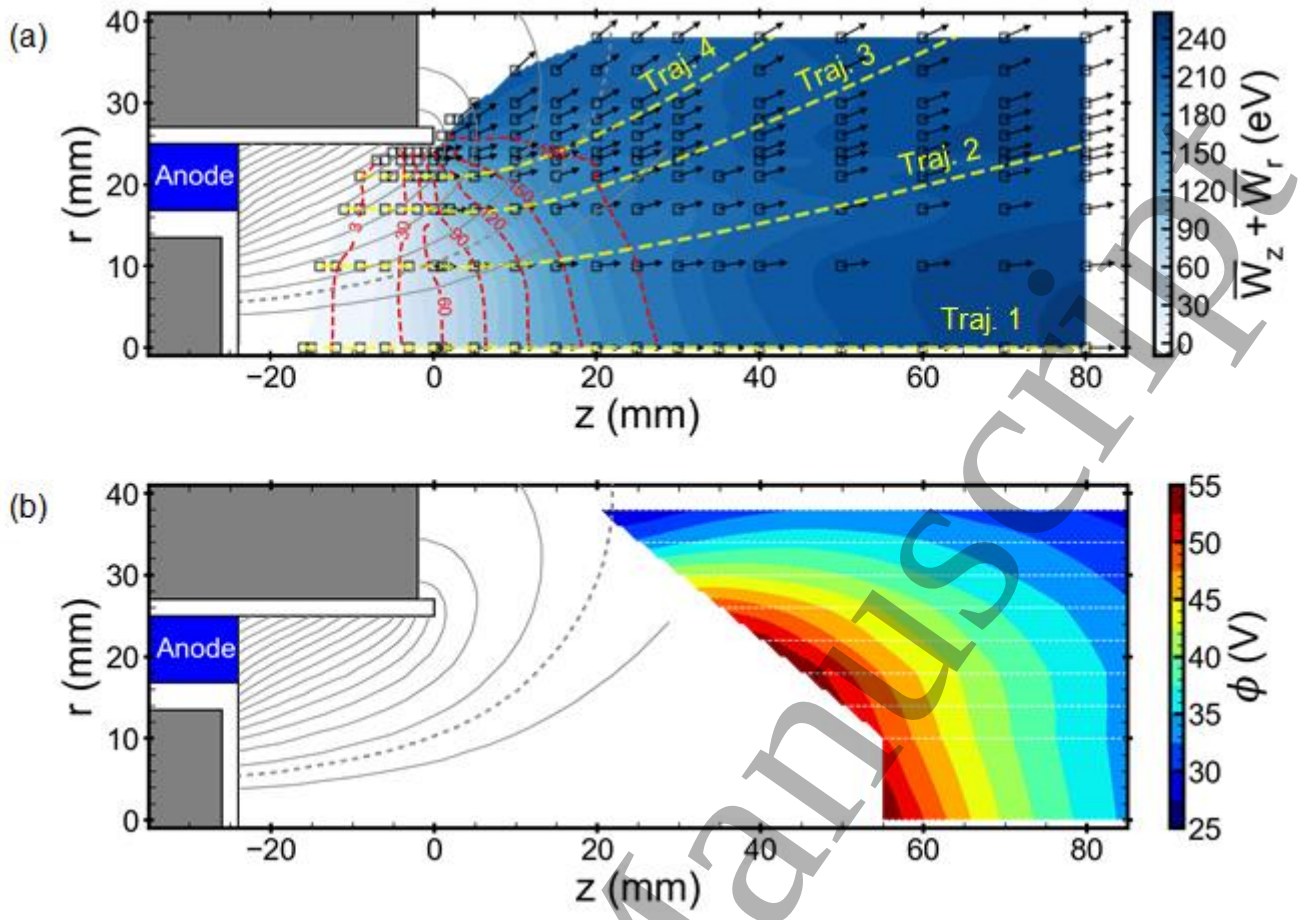

Figure 3. (a) The mean ion velocity vector (arrow) and mean ion energy (color) plot. The red dashed and gray curves are the mean ion energy contour and the magnetic field line, respectively. The squares denote the points where IVDF was measured, and yellow dashed curves are the ion trajectories. (b) The electric potential measured by a floating emissive probe. The cylindrical Hall thruster was operated at 300 V and 7.0 sccm.

To clarify the ion acceleration in the cylindrical Hall thruster plasma, we compared the ion energy profiles along trajectories 1 and 4 with the conventional annular Hall thruster (Fig. 4) that had the same outer channel diameter and depth as the cylindrical Hall thruster [11]. The magnetic field profile of two thrusters can be found in Ref. [21]. For the annular thruster experiment, IVDFs were measured along the centerline of the discharge channel, i.e., r = 21 mm, and the experimental conditions were kept the same (300 V, 280 W). In line with previous observations [1, 18-20], $\overline{W}_z$ increases from z = -5 mm and saturates at approximately z = 10 mm for the annular Hall thruster plasma. On the contrary, the ion acceleration starts at z = -15 mm and saturates at z = 70 mm for trajectory 1. The ion acceleration along trajectory 4 is similar to that in the annular Hall thruster inside the discharge channel. However, outside the discharge channel, it gradually follows the trend of trajectory 1. The reduced axial electron conductivity due to the strong radial magnetic field inside the discharge cavity is probably the cause of the large potential gradient, whereas the rapidly decreasing magnetic field outside the cavity raises the axial electron conductivity and makes the potential gradient similar to trajectory 1. Since the ion acceleration in large radial magnetic fields has been widely studied, we focus here on the acceleration along trajectory 1 where the magnetic field is axially dominant.

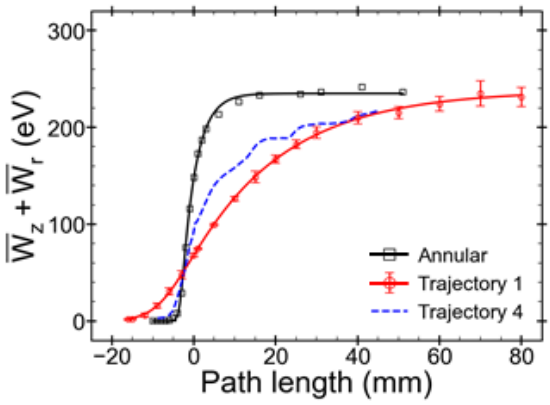

Figure 4. The mean ion energy profile, $\overline{W}_z + \overline{W}_r$, in the annular and cylindrical Hall thrusters having identical channel diameters and depths. Path length = 0 corresponds to the thruster exit plane. The operating conditions were the same, at 300 V anode voltage and 280 W anode power. To keep the same anode power, Xe was supplied at different rates, 10.7 sccm for the annular and 7.0 sccm for the cylindrical thrusters, respectively. Measurement was repeated five times at each location and the error bar indicates a 99% confidence interval.

To confirm the structure of ion acceleration, the ion energy profiles at different anode voltages and flow rates were compared, as shown in Fig. 5. $\overline{W}_r$ was not considered on trajectory 1 since $\overline{W}_r \ll 1$ was maintained. Figure 5(a) shows the axial ion energy profiles obtained at different anode voltages between 200 V to 350 V at 7.0 sccm anode flow rate. As ions accelerate from the thruster cavity, $\overline{W}_z/eV_a$ gradually increases with z and eventually becomes saturated ($\overline{W}_z/eV_a$ = 0.63 to 0.84 at z = 80 mm). With higher V_a, $\overline{W}_z/eV_a$ is higher and this may be attributed to a higher electron temperature [24]. It is noteworthy that $\overline{W}_z/eV_a$ almost monotonically increases with V_a over the entire z range. On the other hand, this monotonic increase is not observed with the Xe mass flow rate ($\dot{m}$) as $\dot{m}$ is increased from 4.0 sccm to 10.0 sccm with V_a = 300 V (Fig. 5(b)). For instance, a comparison between the 5.5 sccm trace (blue) and the 8.5 sccm trace (red) shows that $\overline{W}_z/eV_a$ is lower near the thruster exit for the 8.5 sccm case but it is higher far from the thruster exit plane. The possible reason is as follows. A large propellant flow rate pushes the acceleration front downstream, as can be seen in Fig. 5(b). This is thought to be due to the decrease in electron temperature owing to the large neutral pressure inside the discharge channel [25]. Although probe measurements perturb the discharge [26], the general trend is conserved. In addition, the total ion energy increases when the mass flow rate increases from 4.0 to 7.0 sccm, and then it saturates in the 7.0 to 10.0 sccm range. Thrust, specific impulse, and anode efficiency measurement indicate that the optimal operating range of this thruster is 7.0 – 8.5 sccm. Therefore, the $\overline{W}_z/eV_a$ trend also suggests the optimal operation range of the thruster is above 7 sccm. In conclusion, Fig. 5 clearly demonstrates three facts. First, the acceleration begins at approximately z = -15 mm. Note that the combination of LIF spectroscopy and a floating emissive probe determined the most probable ionization location on the axis as z = -14.9 mm [21]. Second, most of the ion acceleration (more than 70% of the total kinetic energy) occurs outside the discharge channel for a CHT up to 70 mm from the thruster exit, which is 3 times the channel length. Third, the shape of $\overline{W}_z$ profile is robust, i.e. remains almost unchanged, when either the anode voltage or the flow rate is modified.

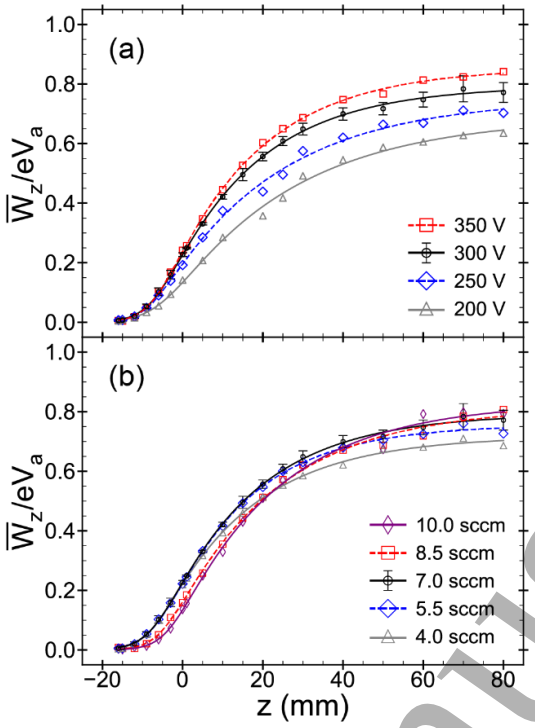

Figure 5. The axial profile of the ion energy and anode voltage ratio ($\overline{W}_z/eV_a$) along trajectory 1 at (a) 7.0 sccm, and (b) 300 V. Most of the ion acceleration took place outside the thruster.

Another important finding is related to the shape of the IVDF, especially the asymmetry on the shape. We first investigated the possible fluorescence line profile broadening factors, which include an isotopic shift, a hyperfine structure, and the Zeeman effect, before analyzing the IVDF [15]. First, the difference in atomic mass of isotopes split the ion velocity. Natural Xe gas is composed of nine stable isotopes [27]. The mean atomic mass is 131.3 and the standard deviation of the atomic mass is 2.1. Therefore, the spread of the ion velocity by the mass should be just within 1% of the mean ion velocity when they undergo the identical electric potential drop. Second, the non-zero nuclear spin of two odd isotopes, ^{129}Xe and ^{131}Xe, at $5d^2F_{7/2}$ state of Xe II ion make additional lines [27]. However, deconvolution of the hyperfine structure does not bring about a noticeable change in the IVDF [28]. Third, the Zeeman splitting is evident when the polarization vector of laser becomes perpendicular to the magnetic field (σ-polarization) [29, 30]. In the case of σ-polarization, the Zeeman splitting linearly increases with the magnitude of magnetic field (slope is 0.23 km/100 G) [30]. However, the energy splitting by the Zeeman effect is symmetrical with respect to the unperturbed energy level. Therefore, the Zeeman effect is not responsible for the asymmetry of the fluorescence line profile. As a result, we speculate that the measured LIF profile of Xe II ion images IVDF well, as shown in many previous studies [15, 28, 31].

In Fig. 2(a), one notable change in the IVDF is the appearance of a high velocity wing when moving downstream. Ion VDF (line profiles) have been fitted to single and double Gaussian. The IVDFs measured at z = -6 mm and 60 mm under the same operating conditions (300 V and 7.0 sccm) are shown in Figs. 6(a) and 6(b), respectively, along with their respective fit. As can be noticed in Fig. 6(a), at z = -6 mm, a single Gaussian fits well to the measured IVDF. At z = 60 mm, a double Gaussian is a good representation of the measured IVDF, as shown in Fig. 6(b). Since each ion group has different velocity and dispersion showing an ion temperature (T_i) in each shifted Gaussian distribution $f(v) \propto \exp(-m(v-v_s)^2/2T_i)$, they are termed as cold and hot ion groups in this paper. The blue dotted and red dashed curves correspond to the cold and the hot ion groups, respectively in Fig. 6(b). Outside the

discharge channel, a double Gaussian matched the measured IVDF with an R-squared (R^2) larger than 0.995. This result implies the existence of two ion populations with different ion temperatures and velocities outside the discharge channel.

Figure 7(a) presents the on-axis profile of the ion temperature of two ion populations. The hot ion group appears just behind the channel exit plane, and its temperature increases up to z = 20 mm and saturates at about 2.5 eV, whereas the temperature of cold ions remains at about 0.4 eV. Figure 7(b) plots the fraction of two ion populations. The cold and hot ion populations were obtained by the areas of the corresponding Gaussian fit, and the fraction was obtained by diving by the entire line shape area. The fraction of the hot ion group increases up to z = 40 mm and saturates at about 0.5, which tends to be similar with its temperature. Figure 7(c) depicts the mean axial velocities of the two ion populations. The average velocity of the hot ion group remained approximately 1 km/s larger than that of the cold ion group.

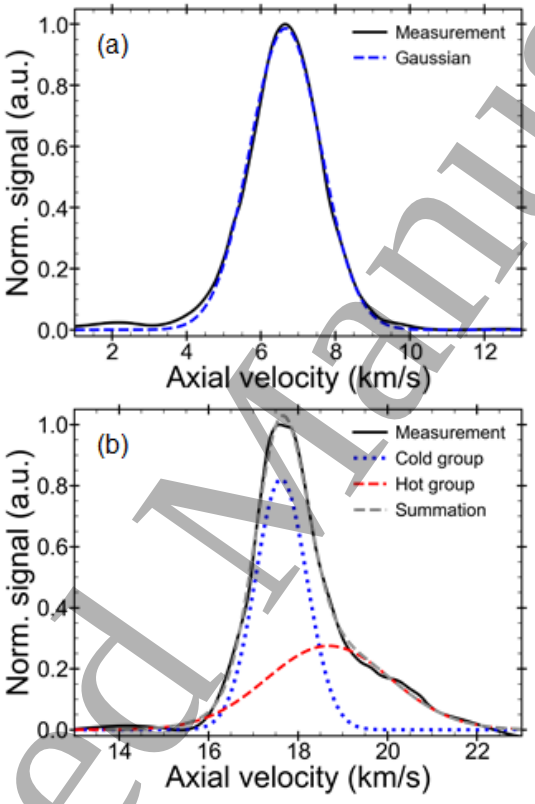

Figure 6. IVDFs fitted with Gaussian distribution at (a) z = -6 mm (single Gaussian), and (b) z = 60 mm (double Gaussian), respectively, at 300 V and 7.0 sccm. The blue dotted and red dashed curves in (b) represent the cold and hot ion groups, respectively. Their summation, denoted in gray, matches well with ($R^2 > 0.995$) the measured IVDF, shown in black.

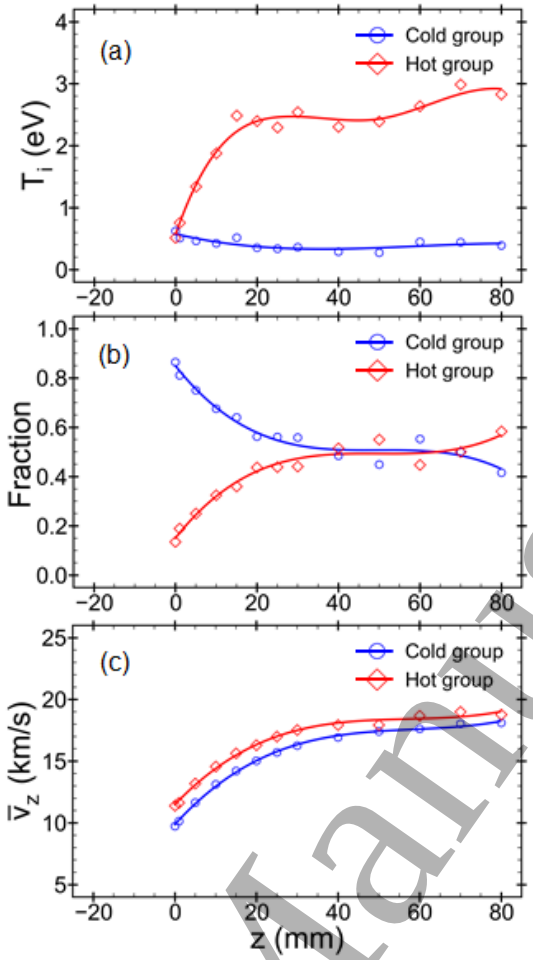

Figure 7. (a) Ion temperature, (b) fractions, (c) and mean axial velocities of the cold and hot ions versus axial distance (300 V and 7.0 sccm).

4. Discussion

We have shown that cylindrical Hall thruster plasmas exhibit a long acceleration region. Possible causes of the extended acceleration region are speculated as follows. A large plasma density was observed upstream of the cylindrical Hall thruster axis [10] and the plasma density would also be large near the axis in the plume since the axially dominant magnetic field does not significantly impede electron transport between the ionization region and the plume. Therefore, electron-ion Coulomb collisions could be considerable as in an end-Hall ion source [32], which has a similar discharge channel geometry and magnetic field topology and may be involved in a long acceleration region. The anomalous collision frequency in the plume, which is two or three orders of magnitude larger than the classical collision frequency [33], and magnetic mirroring in the upstream region may also be responsible for the gentle and extended potential gradient in the cylindrical Hall thruster plasma.

In order for the ion energy in the plume to reach about $0.8V_a$ (Fig. 5(b)), the upstream potential needs to be close to V_a. However, for the near-axis, the magnetic field near the thruster axis does not pass through the anode (Fig. 1(a)), and therefore a large upstream potential could not be guaranteed. The previous study confirmed that the off-axis cathode establishes an increasing electric potential toward the thruster axis and prevents radial electron outflux

in order to maintain the quasi-neutrality [34], and the increase of potential toward the axis is also shown in the cylindrical Hall thruster (Fig. 3(b)). Therefore, we believe that the off-axis mounted cathode attributes to the formation of high upstream potential on the axis and enables the large ion energy in the plume.

The charge exchange collision and plasma instabilities can be the cause of the asymmetry of IVDF. First, regarding the charge exchange collisions, the charge exchange collision cross-section between Xe II and Xe I does not exceed 1×10^{-18} m^2 [35]. By assuming the neutral density of about 10^{18} m^{-3} outside the discharge cavity, the mean free path, $l = (\sigma_{\mathrm{CX}} n)^{-1}$, becomes about 1 m, which is much larger than the plume plasma size. Therefore, the charge exchange collisions are considered to play a minor role in the shape of the IVDFs. Second, the Xe II IVDF can be broadened by the ion-ion two stream instability (IITSI), which is the axially formed MHz scale instability that is established by the significant fraction of the multiply charged ions and the velocity difference between Xe II and multiply charged Xe ions [36, 37]. The fraction of the multiply charged ion density on the axis of the cylindrical Hall thruster was measured as 37%, and this amount is large enough to promote IITSI. Third, previous studies reported that the appearance of the fast ions was accompanied by the observation of a strong ion transit time instability (ITTI) [38-41] in the 100-500 kHz range. About 350 kHz oscillations were consistently observed in the discharge current during the experiment, and asymmetry in IVDF appeared with a hot ion population near the thruster axis. In addition, numerical simulations reported that ITTI broadens IVDF by generating not only fast ions but also very slow ions [40, 41], which were also observed in Fig. 2(a). Both IITSI and ITTI can appear with sufficiently high ion velocity and can be significant after the ions undergo a sufficiently high potential drop. The hot ion group became noticeable beyond $z = 0$ mm where $\bar{W}_z$ is 68 eV, and its temperature was increased until they reach $z = 20$ mm where $\bar{W}_z$ is 167 eV in this experiment (Fig. 3). Therefore, we believe that the results are reasonably consistent with this postulate. We attempted to separate the oscillations and multiply charged ion fraction by adjusting operation conditions. However, changes in the oscillations and multiply charged ion fraction occurred simultaneously. Additional studies are required to answer the question on the origin of the hot ions observed in our experiment.

5. Summary and conclusion

The structure of the ion acceleration region and the shape of the IVDF of a cylindrical Hall thruster using LIF spectroscopy were studied. The ion energy profiles measured at various anode voltages and flow rates demonstrated that the acceleration structure was established between 15 mm inside and 70 mm outside the discharge channel, which is 3-4 times the channel length along the thruster axis, regardless of the discharge condition. Also, most of the ion acceleration (more than 70% of its maximum energy) took place outside the discharge channel. This trend was maintained under different experimental conditions, and this extended ion acceleration region was most evident along the thruster axis where the magnetic field is axially dominant.

On the thruster axis, the measured IVDFs were fitted well with a single Gaussian inside the discharge channel. However, double Gaussian fitting, representing the cold and hot ion groups, described the measured IVDFs well outside the channel, indicating the existence of cold and hot ion groups. The ion temperature and population of the hot ion group gradually increased from the thruster exit and its fraction became almost half at $z > 40$ mm.

Data availability statement

The data that support the findings of this study are available upon reasonable request from the authors.

Acknowledgments

Authors would like to appreciate Prof. Z. Ning at Harbin Institute of Technology for providing hollow cathodes. This work was partially supported by the Space Core Technology Program (Grant No. 2014M1A3A3A02034510) and Space Pioneer Program (Grant. No. NRF-2021M1A3B9096775) via the National Research Foundation of Korea, funded by the Ministry of Science and ICT, Republic of Korea.

References

[1] Mazouffre S, Kulaev V and Luna J P 2009 Ion diagnostics of a discharge in crossed electric and magnetic fields for electric propulsion *Plasma Sources Sci. Technol.* **18** 034022

[2] Reid B M 2009 The influence of neutral flow rate in the operation of Hall thrusters *Ph.D. Dissertation* Aerospace Engineering University of Michigan, Ann Arbor, Michigan, USA

[3] Gawron D, Mazouffre S, Sadeghi N and Heron A 2008 Influence of magnetic field and discharge voltage on the acceleration layer features in a Hall effect thruster *Plasma Sources Sci. Technol.* **17** 025001

[4] Grimaud L and Mazouffre S 2017 Ion behavior in low-power magnetically shielded and unshielded Hall thrusters *Plasma Sources Sci. Technol.* **26** 055020

[5] Garrigues L, Santhosh S, Grimaud L and Mazouffre S 2019 Operation of a low-power Hall thruster: comparison between magnetically unshielded and shielded configuration *Plasma Sources Sci. Technol.* **28** 034003

[6] Mikellides I G, Katz I, Hofer R R and Goebel D M 2013 Magnetic shielding of walls from the unmagnetized ion beam in a Hall thruster *Appl. Phys. Lett.* **102** 023509

[7] Mazouffre S, Tsikata S and Vaudolon J 2014 Development and experimental characterization of a wall-less Hall thruster *J. Appl. Phys.* **116** 243302

[8] Raitses Y and Fisch N J 2001 Parametric investigations of a nonconventional Hall thruster *Phys. Plasmas* **8** 2579

[9] Smirnov A, Raitses Y and Fisch N J 2004 Electron cross-field transport in a low power cylindrical Hall thruster *Phys. Plasmas* **11** 4922

[10] Smirnov A, Raitses Y and Fisch N J 2007 Experimental and theoretical studies of cylindrical Hall thrusters *Phys. Plasmas* **14** 057106

[11] Kim H, Lim Y, Choe W and Seon J 2014 Effect of multiply charged ions on the performance and beam characteristics in annular and cylindrical type Hall thruster plasmas *Appl. Phys. Lett.* **105** 144104

[12] Spektor R, Diamant K D, Beiting E J, Raitses Y and Fisch N J 2010 Laser induced fluorescence measurements of the cylindrical Hall thruster plume *Phys. Plasmas* **17** 093502

[13] Kim H, Lim Y, Choe W, Park S and Seon J 2015 Effect of magnetic field configuration on the multiply charged ion and plume characteristics in Hall thruster plasmas *Appl. Phys. Lett.* **106** 154103

[14] Cedolin R J, Hargus W A, Storm P V, Hanson R K and Cappelli M A 1997 Laser-induced fluorescence study of a xenon Hall thruster *Appl. Phys. B* **65** 459

[15] Mazouffre S 2013 Laser-induced fluorescence diagnostics of the cross-field discharge of Hall thrusters *Plasma Sources Sci. Technol.* **22** 013001

[16] Hargus W A and Cappelli M A 2001 Laser-induced fluorescence measurements of velocity within a Hall discharge *Appl. Phys. B* **72** 961

[17] Chaplin V H, Conversano R W, Lobbia R B, Ortega A L, Mikellides I G, Hofer R R and Jorns B A 2017 Laser-Induced Fluorescence Measurements of the Acceleration Zone in the 12.5 kW HERMeS Hall Thruster *35th International Electric Propulsion Conference* IEPC-2017-229 *(Atlanta, Georgia, USA)*

[18] Mazouffre S, Gawron D, Kulaev V and Sadeghi N 2008 Xe(+) Ion Transport in the Crossed-Field Discharge of a 5-kW-Class Hall Effect Thruster *IEEE Trans. Plasma Sci.* **36** 1967

[19] Hargus W A and Nakles M R 2008 Ion Velocity Measurements Within the Acceleration Channel of a Low-Power Hall Thruster *IEEE Trans. Plasma Sci.* **36** 1989

[20] MacDonald-Tenenbaum N, Pratt Q, Nakles M, Pilgram N, Holmes M and Hargus W 2019 Background Pressure Effects on Ion Velocity Distributions in an SPT-100 Hall Thruster *J. Propuls. Power* **35** 403

[21] Doh G, Park J, Lee D, Kim H and Choe W 2021 Determination of the ionization region in Hall thruster plasmas with low perturbation *J. Appl. Phys.* **130** 193301
[22] Simmonds J and Raitses Y 2021 Ion acceleration in a wall-less Hall thruster *J. Appl. Phys.* **130** 093302
[23] Fisch N J, Raitses Y and Fruchtman A 2011 Ion acceleration in supersonically rotating magnetized-electron plasma *Plasma Physics and Controlled Fusion* **53** 9
[24] Raitses Y, Staack D, Keidar M and Fisch N J 2005 Electron-wall interaction in Hall thrusters *Phys. Plasmas* **12** 057104
[25] Reid B M and Gallimore A D 2008 Langmuir probe measurements in the discharge channel of a 6-kW Hall thruster *44th AIAA/ASME/SAE/ASEE Joint Propulsion Conference & Exhibit* AIAA-2008-4920 *(Hartford, Connecticut, USA)*
[26] Grimaud L, Petin A, Vaudolon J and Mazouffre S 2016 Perturbations induced by electrostatic probe in the discharge of Hall thrusters *Rev. Sci. Instrum.* **87** 043506
[27] Pawelec E, Mazouffre S and Sadeghi N 2011 Hyperfine structure of some near-infrared Xe I and Xe II lines *Spectroc. Acta Pt. B-Atom. Spectr.* **66** 470
[28] Huang W, Smith T B and Gallimore A D 2009 Obtaining Velocity Distribution using a Xenon Ion Line with Unknown Hyperfine Constants *40th AIAA Plasmadynamics and Lasers Conference* AIAA 2009-4226 *(San Antonio, Texas, USA)*
[29] Smith T B, Huang W, Ngom B B and Gallimore A D 2007 Optogalvanic and laser-induced fluorescence spectroscopy of the Zeeman effect in xenon *30th International Electric Propulsion Conference* IEPC-2007-229 *(Florence, Italy)*
[30] Huang W 2011 Study of Hall Thruster Discharge Channel Wall Erosion via Optical Diagnostics *Ph.D. Dissertation* Aerospace Engineering University of Michigan, Ann Arbor, Michigan, USA
[31] W. A. Hargus J and Nakles M R 2006 Evolution of the Ion Velocity Distribution in the Near Field of the BHT-200-X3 Hall Thruster *42nd AIAA/ASME/SAE/ASEE Joint Propulsion Conference* AIAA-2005-4991 *(Sacramento, CA)*
[32] Oudini N, Hagelaar G J M, Boeuf J P and Garrigues L 2011 Physics and modeling of an end-Hall (gridless) ion source *J. Appl. Phys.* **109** 073310
[33] Mikellides I G and Ortega A L 2019 Challenges in the development and verification of first-principles models in Hall-effect thruster simulations that are based on anomalous resistivity and generalized Ohm's law *Plasma Sources Sci. Technol.* **28** 014003
[34] Oudini N, Garrigues L, Hagelaar G J M and Boeuf J P 2012 Numerical study of the characteristics of the ion and fast atom beams in an end-Hall ion source *J. Appl. Phys.* **112** 8
[35] Miller J S, Pullins S H, Levandier D J, Chiu Y and Dressler R A 2002 Xenon charge exchange cross sections for electrostatic thruster models *J. Appl. Phys.* **91** 984
[36] Hara K and Tsikata S 2020 Cross-field electron diffusion due to the coupling of drift-driven microinstabilities *Phys. Rev. E* **102** 023202
[37] Tsikata S, Cavalier J, Heron A, Honore C, Lemoine N, Gresillon D and Coulette D 2014 An axially propagating two-stream instability in the Hall thruster plasma *Phys. Plasmas* **21** 072116
[38] Lim Y, Kim H, Park J, Choe W, Mazouffre S, Seon J and Garrigues L 2017 Nonlinear ion dynamics in Hall thruster plasma source by ion transit-time instability *Plasma Sources Sci. Technol.* **26** 03LT01
[39] Vaudolon J and Mazouffre S 2015 Observation of high-frequency ion instabilities in a cross-field plasma *Plasma Sources Sci. Technol.* **24** 032003
[40] Bareilles J, Hagelaar G J M, Garrigues L, Boniface C, Boeuf J P and Gascon N 2004 Critical assessment of a two-dimensional hybrid Hall thruster model: Comparisons with experiments *Phys. Plasmas* **11** 3035
[41] Hagelaar G J M, Bareilles J, Garrigues L and Boeuf J P 2003 Role of anomalous electron transport in a stationary plasma thruster simulation *J. Appl. Phys.* **93** 67